Trends in Optics and Photonics Vol. 24, Fabrication and Testing of Aspheres, (Optical Society of America, Washington, DC) 1999.

Testing extreme ultraviolet optical systems at-wavelength with sub-angstrom accuracy

Kenneth A. Goldberg

Center for X-Ray Optics, Lawrence Berkeley National Laboratory,
Mail Stop 2-400, LBNL, Berkeley, CA 94720

1. Abstract

Achieving diffraction-limited performance from extreme ultraviolet (EUV) optical systems requires the development of interferometry with sub-angstrom accuracy. At-wavelength EUV testing with a phase-shifting point diffraction interferometer is being developed for the measurement of lithographic quality, multiple-element, aspherical optical systems. Recent demonstrations of high-accuracy EUV interferometry, and progress in this field, have required detailed analysis and *in situ* calibration of systematic errors generated by the measurement geometry. The framework of this detailed analysis is presented along with recent measurements and a discussion of concomitant metrologies made available by the interferometer.

Key Words

(120.3180) Interferometry; (260.7200) Ultraviolet, extreme; (120.6650) Surface measurements, figure.

2. Introduction

EUV lithography is a promising and viable candidate for circuit fabrication with 0.1-micron critical dimension and smaller. To achieve this end at 11 to 13-nm wavelength, nearly diffraction-limited, multilayer-coated, near-normal-incidence reflective optical systems with 0.1 numerical aperture (NA) are required [1]. The suggested wavefront aberration tolerance for these sophisticated, all-reflective systems, which are composed of multiple aspherical elements, is only 0.02 waves rms, or 0.27 nm [1]. This places extremely high demands on the fabrication of EUV mirror substrates and multilayer coatings, and even higher demands on the metrology tools required to characterize them.

The EUV wavefront is determined by the geometric figure of the mirror surfaces and by the properties of the multilayer coatings, which are deposited across mirror areas covering many square inches. While advanced visible-light interferometric techniques possessing the required measurement accuracy are being developed [3, 4], at-wavelength EUV testing is the most direct probe of the sensitive resonance properties of reflective multilayer coatings. The need for at-wavelength metrology has motivated the development of high-accuracy EUV wavefront-measuring interferometry.

Since modern optical imaging systems often incorporate aspherical elements, opportunities for EUV single-element or convex-element testing are extraordinarily challenging. In reflection, each micron of aspherical departure represents more than 150 EUV wavelengths. As a result EUV interferometry is presently restricted to system-level wavefront measurement.

Several different EUV interferometers have been developed over the past decade. Foucault [5] and Ronchi [6] testing for alignment of EUV optics have been demonstrated using both synchrotron [7] and laser-plasma [8] light sources. Other significant research includes refinement of the lateral shearing interferometer [9], and the point-diffraction interferometer (PDI) [10, 11, 12].

The most successful of the EUV interferometers to date has been the recently developed phase-shifting point diffraction interferometer (PS/PDI), first proposed by Medecki [13]. While the PS/PDI preserves the advantages of the PDI, using pinhole diffraction to generate a spherical reference wavefront in the image plane, it represents a significant step forward. With substantially higher efficiency and the introduction of phase-shifting capability, the PS/PDI has become one of the most accurate system-level measurement tools of its kind. Its reference wavefront accuracy has been demonstrated as high as 0.04 nm rms in a numerical aperture of 0.08, well beyond the present

requirements for EUV optical system metrology.

Successful operation of an interferometer for which angstrom-scale errors are unacceptably large requires diligent attention to minute details of the measurement. This article is devoted to attaining the highest possible measurement accuracy with the PS/PDI. To that end, the many free parameters of the PS/PDI design are investigated, including discussion of the most significant design compromises. Accompanying the qualitative design discussions is a detailed study of the most significant systematic errors sources affecting the PS/PDI. A mathematical framework is developed in which these errors are translated into the familiar Zernike polynomial representation, commonly used in the description of optical aberrations.

These theoretical studies have fed back into the experimental methods, improving the quality and reliability of the measurements. Recent EUV PS/PDI optical system measurements are presented along with a discussion of related measurement capabilities and future directions for research.

3. The phase-shifting point diffraction interferometer

The PS/PDI was designed specifically to measure EUV imaging systems with sub-nanometer accuracy, yet its simple design and operating principles give it potential for application in a broad range of circumstances. The PS/PDI relies on pinhole diffraction to produce high-accuracy spherical wavefronts, overcoming the unavailability of adequate reference surfaces. A common-path design allows it to operate with illumination sources of limited temporal coherence.

As shown in Fig. 1, the PS/PDI uses a pair of pinholes placed at conjugate object and image points to produce spherical reference wavefronts. The *object pinhole* spatially filters the incident light to produce a spherical illuminating beam. Via transmission the illuminating beam acquires the aberrations of the test optic and becomes the *test beam*. The test beam comes to focus in the image plane and then propagates to reach the detector, which is placed significantly beyond the image plane.

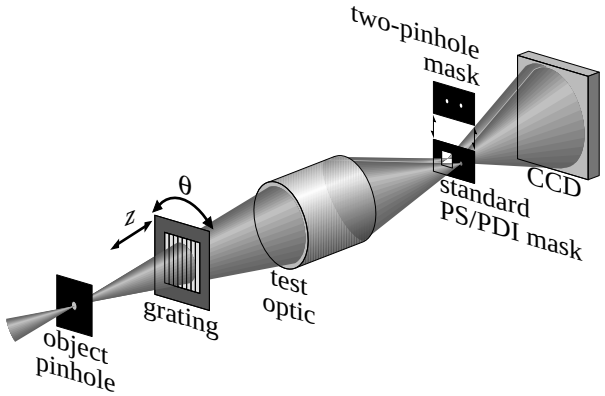

Figure 1. Schematic optical design of the phase-shifting point diffraction interferometer. Two different image-plane masks are shown.

To create the *reference beam*, a small-angle beam splitter is placed before (or after) the test optic; a relatively coarse transmission grating makes a convenient beam splitter for this application. The grating produces multiple copies of the test beam, focused in the image plane with a small lateral separation. A patterned opaque membrane in the image plane is used to selectively transmit and block the focused beams. One of these beams is transmitted through a relatively large "window" and becomes the test beam. A second beam is brought to focus on a nearby pinhole spatial filter called the *reference pinhole*. The reference pinhole is fabricated smaller than the diffraction-limited resolution of the test optical system to produce a second spherical reference wavefront. The two beams propagate to a mixing plane, where their coherent interference is recorded by a suitable array detector.

3.1 Efficiency

Due to the limited brightness of available EUV sources, an interferometer's efficiency is an important design consideration. Efficiency can be defined as the relative fraction of the illuminating light that reaches the detector, including or excluding transmission through the test optic. Efficiency determines detector exposure times during both alignment and measurement and is therefore integral to the operation of the interferometer.

Pinhole spatial filtering plays the dominant role in setting the efficiency of the PS/PDI. Above all other factors, the pinholes dictate the accuracy and precision of the measurement. Smaller pinholes generate higher-quality reference beams at the expense of transmission. Coupled to the focusing quality of the test optic, pinhole size selection mandates a compromise between throughput and accuracy.

While efficiency determines exposure time, achieving a high signal-to-noise ratio in wavefront measurements relies primarily on interference fringe contrast. High contrast, guaranteed by balancing the intensities of the test and reference beams, requires special consideration in the PS/PDI. The potentially severe loss of flux from spatial filtering in the image plane can create a significant imbalance of power between the test and reference beams.

To alleviate the imbalance, several PS/PDI efficiency improvements have been proposed or demonstrated. The intrinsic power difference between adjacent diffraction orders of a grating beam splitter gives the test and reference beams different intensities in the image plane. This fact creates an opportunity to control their relative intensities. For example, the loss incurred by transmission through the reference pinhole can be compensated by selecting the *stronger* of two beams (typically the zeroth-order) as the reference beam. Under this principle, gratings designed with high duty-cycles (ratio of transparent to opaque areas)

can be tailored to match the two beam intensities as desired [14]. The higher duty-cycle also improves the efficiency of the interferometer.

3.2 Mask design

As described above, the PS/PDI image-plane mask transmits the test beam through a relatively large window, spatially filters the reference beam with a small pinhole, and blocks all other orders from the grating beam splitter. Designing a mask to satisfy these three criteria affords a great deal of freedom. Among the free parameters are the window's size and shape, and the pinhole-to-window separation. Examples of three PS/PDI mask designs are shown in Fig. 2.

Although it should be designed many times larger than the diffraction-limited focal spot size, the window nonetheless acts as a spatial filter: its size determines the highest spatial frequencies and the degree of wavefront curvature preserved in the test beam.

When properly configured, the mask should be designed for the test beam to pass through the center of the window when the reference beam is aligned on the reference pinhole. The distance from the pinhole to the window's center (equivalent to the beam-separation distance) should be chosen large enough to minimize overlapping of the adjacent beams. Of particular concern is the transmission, or *leakage*, of unwanted light through the open window. Although the other beams are displaced from the test beam's window, the window behaves as a bandpass filter and transmits high-spatial-frequency components from the nearby beams. If not properly filtered, these components can create confusion in the fringe analysis [15].

Beam overlap constrains the window size only in the direction of beam separation. In principle, there is no limit to the length of the window in the orthogonal direction; one advantage of extending the window's length is an increase in spatial-frequency resolution in that direction [16]. This point is discussed in Section 6.

In the original design of the PS/PDI [13, 17], a square window was used with a beam separation equal to the window's width. A slightly more restrictive window-size prescription has recently been introduced to improve the noise-immunity of the interferometer. In order to guarantee the Fourier spatial-frequency-domain separability of the test and reference beams, the *dual-domain* configuration requires that the window width not exceed two-thirds of the beam-separation distance [15].

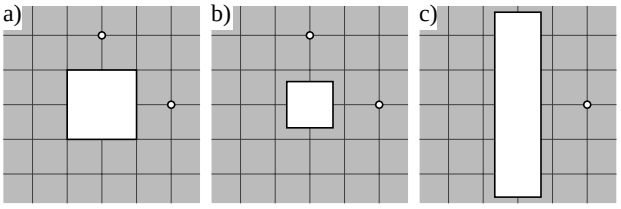

Figure 2. Three image-plane mask designs. **(a)** The original design with equal window width and beam separation. The second pinhole allows rotation of the beam separation direction. **(b)** Reduced window size minimizes beam overlap. **(c)** Window elongation extends the mid-spatial-frequency response in one direction.

3.3 Grating pitch and placement

The PS/PDI offers considerable latitude in the position of the grating beam splitter. The beam splitter may be placed between the object plane and the test optic, between the test optic and the image plane, or ahead of the object plane. These positions are illustrated in Fig. 2. The first two configurations are very similar in efficiency and operation. The third configuration requires that similar window/pinhole masks be placed in both the object and image planes. In this special case, the test and reference beams are separated in advance of the object plane. The test beam is spatially filtered in the object plane, while the reference beam is spatially filtered in the image plane. The windows transmit the unfiltered beams through the object and image planes, respectively. By filtering the reference beam only once, rather than twice, the efficiency of this configuration can be higher than in conventional PS/PDI designs. However, since successful implementation requires that the test and reference beams be fully separable in the object plane, this arrangement is limited to situations in which the illuminating beam can form a high-quality point image.

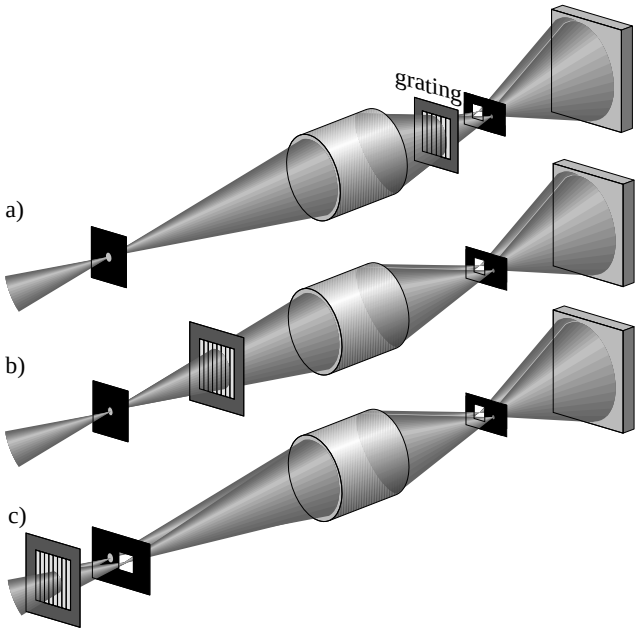

Figure 3. The grating beam splitter may occupy a range of positions, with advantages and disadvantages to each. Positions shown in **(a)** and **(b)** have identical efficiency considerations. **(c)** affords much higher efficiency but requires beam separability in the object plane.

Within each configuration, a range of positions is available to the grating. It is easily shown that, independent of the illumination wavelength, the number of grating lines illuminated within the NA of interest is equivalent to the number of fringes that appear in the measured interference pattern [16]. Once a desired beam-separation distance is chosen for the image plane, the grating's pitch and its distance from one of the conjugate planes become dependent parameters, linked by a constant ratio.

In some cases, the grating pitch and position may be limited by the *shear angle* between the test and reference beams. The shear angle varies only with the pitch of the grating and the wavelength. If the grating is placed very close to one of the conjugate planes, then the pitch must be reduced to compensate, and the resultant increase in the shear angle may reduce the useful overlap of the beams.

Here it is essential to recognize that the spherical quality of pinhole-diffracted beams decreases with the solid angle under consideration. That is, diffracted wavefronts have arbitrary quality over only a finite angular range. When the shear angle is large relative to the beam divergence, reference-wave quality may be compromised. It is therefore advisable in practice to restrict the shear angle to a small fraction of the illumination angle.

3.4 Beam alignment and position control

The most challenging aspect of using the PS/PDI is the requisite pinhole alignment in the object and image planes. Today's diffraction-limited lithographic optics are designed to produce beam profiles on the order of 100–200 nm across. Testing these systems requires the fabrication and control of sub-100-nm pinholes with sub-50-nm positioning. Coupled with millimeter-scale translation requirements, this level of precision and control places strict demands on stage motion and measurement.

4. Compensable systematic errors

In pursuit of the highest attainable accuracy, it is essential that every element of the interferometer, including the measurement geometry, be considered as a potential source of systematic errors. By definition, systematic errors are those that can be removed after an appropriate calibration (if available) is performed. This section contains a mathematical description of the most significant systematic error sources affecting the PS/PDI. Errors related to the path-length difference in the measurement geometry are additive and, once understood, can be subtracted. Errors related to the detection geometry must be compensated mathematically.

Not discussed in this article are random error sources (from vibration, e.g.), errors related to inadequate pinhole spatial filtering, or errors related to the detection of the interference pattern and the subsequent fringe-pattern analysis. These and many other sources of measurement uncertainty are shared by most interferometers and do not warrant special coverage here.

4.1 Alignment

Common to all interferometers but worth mention is the importance of alignment. Any optical design has some tolerance to the location of the conjugate object and image points in imaging or wavefront measurement. Yet even with the individual elements of a compound system placed in perfect *relative* alignment, mislocation of the measurement points will introduce an apparent systematic error. A system's tolerance to conjugate point location is what defines its field of view. To ensure the usefulness of interferometry, great effort must be made to ensure that an optic is measured in the same way it is used.

4.2 Uniform coordinate system

To facilitate the analyses presented in this chapter, a uniform set of coordinates will be used, as shown in Fig. 4. We place the origin at one of the conjugate points; this is the test beam's center of curvature. The beam propagates with its central ray coincident with the *z*-axis. The cylindrically symmetric cone of rays subtending the NA has a half-angle α such that $\mathrm{NA} \equiv \sin\alpha$. Because the tangent of α is also used, we define $t \equiv \tan\alpha$. θ is the spherical polar coordinate defined from the *z*-axis.

Lateral displacement from the optic axis is defined by the cylindrical polar coordinate vector **r,** defined as $\mathbf{r} \equiv (r\cos\phi, r\sin\phi)$. In the image plane, where the test and reference beams are focused, the beam-separation vector **s** is defined as $\mathbf{s} \equiv (s\cos\phi_s, s\sin\phi_s)$.

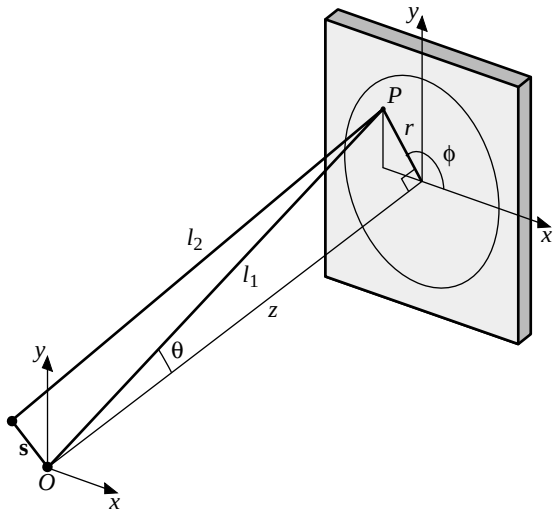

Figure 4. Coordinate systems used in the systematic error analyses, shown from the image plane to the detector. The origin is defined at the test beam focus in the image plane, and the z-axis is coincident with the central ray. The displaced reference pinhole is located at **s** in the image plane. The distance from the origin to the detector along the central ray is *z*.

4.3 Zernike polynomials

The final step in the analysis of a systematic error is representation in terms of the Zernike polynomials, defined on the unit circle [18, 19, 20]. For this step, we define a polar coordinate pair (ρ, ϕ), where the normalized radius ρ is related to the scalar r by $\rho \equiv r/r_{max}$. It should be clear from the geometry that $r_{max} = zt$.

There are many conventions available for the representation of the Zernike polynomials. These conventions most commonly differ in the sequence and the values of the leading coefficients. We will work with the orthogonal Zernike set $\{Z_n \equiv Z_n(\rho, \phi)\}$ bounded on the range [-1, 1], and defined as follows. The named, lowest-ordered aberration terms are piston, tilt, defocus, astigmatism, coma, spherical aberration, and triangular astigmatism.

piston	$Z_0 = 1$	coma	$Z_6 = (3\rho^2 - 2\rho)\cos\phi$
x-tilt	$Z_1 = \rho\cos\phi$	coma	$Z_7 = (3\rho^2 - 2\rho)\sin\phi$
y-tilt	$Z_2 = \rho\sin\phi$	sph. ab.	$Z_8 = 6\rho^4 - 6\rho^2 + 1$
defocus	$Z_3 = 2\rho^2 - 1$	tri. astig.	$Z_9 = \rho^3\cos 3\phi$
astig.	$Z_4 = \rho^2\cos 2\phi$	tri. astig.	$Z_{10} = \rho^3\sin 3\phi$
45° astig.	$Z_5 = \rho^2\sin 2\phi$		

4.4 Geometric coma

The image-plane separation of the test and reference beams generates a wavefront tilt that is responsible for the characteristic pattern of parallel fringes in PS/PDI interferograms. Independent of optical aberrations that may be present in the test optic, consideration of the path-length difference reveals a series of higher-ordered coma components that are referred to as the *geometric coma*. The magnitude of coma varies linearly with the image-plane beam separation **s** and with the third-power of the NA. In this section, an expression for the coma is introduced and two solutions for its removal are proposed.

The detector is located a distance z from the image plane. A measurement point P in the detector plane is represented by the position **r**. Defining l_1 as the distance from the origin to P, and l_2 as the distance from the reference beam center to P, we have

$$l_1 = \sqrt{z^2 + r^2}$$
$$l_2 = \sqrt{z^2 + r^2 + s^2 - 2rs\cos(\phi - \phi_{\mathbf{s}})}. \qquad (1)$$

In addition to aberrations in the test beam, the geometric path-length difference Δl produces the interference pattern. Expanding the difference $\Delta l = l_1 - l_2$ up to third order in r and to first order in s yields the first higher-ordered correction,

$$\Delta l = \frac{s}{z} r\cos(\phi - \phi_{\mathbf{s}}) - \frac{s}{2z^3} r^3\cos(\phi - \phi_{\mathbf{s}}). \qquad (2)$$

Using the substitution $r = tz\rho$, we can insert the Zernike polynomials for tilt and coma:

$$\Delta l = st\left(1 - \tfrac{1}{3}t^2\right)Z_1(\rho, \phi - \phi_{\mathbf{s}}) - \tfrac{1}{6}st^3 Z_6(\rho, \phi - \phi_{\mathbf{s}}). \qquad (3)$$

Alone, the path-length difference attributable to the geometric coma Δl_{geom} is

$$\Delta l_{geom} = -\tfrac{1}{6}st^3 Z_6(\rho, \phi - \phi_{\mathbf{s}}). \qquad (4)$$

The tilt and coma coefficients are linked by a constant relationship dependent only on t. Using C and T as the coma and tilt coefficients, respectively, we can write

$$C = -\frac{t^2}{6 - 2t^2} T. \qquad (5)$$

This relationship holds for both of the paired components of the tilt and coma simultaneously.

This known proportionality can be exploited to identify and remove the geometric coma. If the NA is precisely known (and hence t as well), then the coma can be inferred from the measured tilt. When the NA is not well known, a solution cannot be deduced from a single measurement; two or more measurements are required. Notice that the coma and tilt terms are proportional to and aligned with the beam-separation vector **s**. Therefore, by using a combination of different beam-separation magnitudes or directions, the underlying "true" wavefront can be separated from the geometric coma effect [16]. Enabling this measurement is one purpose of the

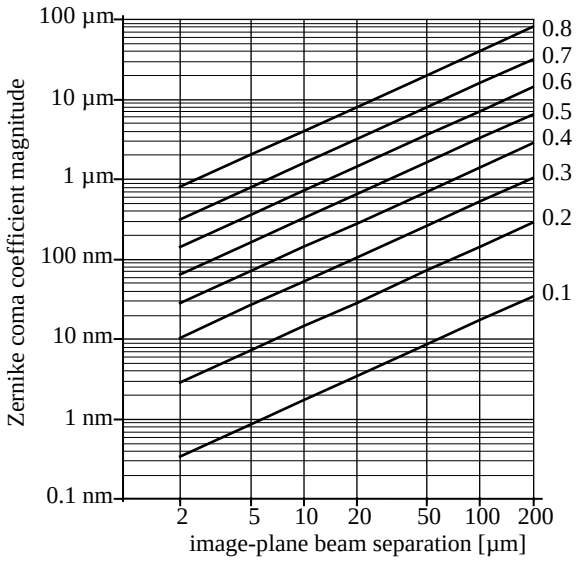

Figure 5. The magnitude of the geometric coma systematic error varies with the beam separation **s** and approximately with NA^3. Shown are Zernike coma coefficient magnitudes for NA values between 0.1 and 0.8 with a range of reasonable beam separations.

two-reference-pinhole configuration of the PS/PDI image-plane mask.

In Fig. 5, the Zernike coefficient magnitude of the geometric coma error is shown for a range of numerical apertures and beam separations. Based on the measurement geometry alone, these coefficient magnitudes are independent of the illuminating wavelength.

4.5 Grating coma

Another potentially significant systematic error at moderate NA comes from the use of a planar grating beam splitter in a spherically diverging or converging beam. Since the angles of incidence vary across the illuminated region of the grating, a small phase error is introduced into the diffracted beams. In a geometric description, the grating pitch appears reduced to the off-axis rays perpendicular to the grating rulings. This leads to a variation in the grating's diffraction angle within the cone of the beam, referred to as the *grating coma*.

Since the grating coma affects only diffracted orders from the grating beam splitter, and not the zeroth-order beam, this error source can be eliminated completely. By using the first-order beam as the reference beam, any coma introduced into the reference wave will be spatially filtered and removed. However, owing to concerns about the efficiency of the interferometer it is usually disadvantageous to use the first-order beam as the reference.

We derive an expression for this systematic error using Babinet's principle [21], treating the grating diffraction as an inverse problem. That is, given a spherical illuminating wavefront incident on a grating of pitch d, we determine the aspherical phase of a second wavefront that could interfere with the first to produce the uniform-pitch grating pattern.

We can solve the problem in a general manner without regard to whether the incident beams are converging or diverging: we define the path-length $R(\theta, \phi)$ from the source point to an arbitrary point on the grating. k is the wavevector of the illumination, $k \equiv 2\pi/\lambda$, and κ is a wavevector describing the grating, $\kappa \equiv 2\pi/d$, aligned in an arbitrary direction. The appropriate Zernike polynomial representation for wavefront aberrations is the spherical coordinate system of the beam, not a circle in a plane. Once an expression for the unknown phase is derived, the normalized polar angle will take the place of the radial parameter ρ.

Using θ as the polar angle from the source to the point on the grating, ϕ as the azimuthal angle about the central ray, and ϕ_s as the grating orientation, an expression for the unknown phase Φ may be written as follows:

$$kR - \Phi = \kappa r \cos(\phi - \phi_s). \quad (6)$$

The grating angle ϕ_s, defined normal to the rulings, both determines and is parallel to the beam-separation vector $\mathbf{s}$. Dividing through by k, the corresponding path-length difference Δl is

$$\Delta l = R - \frac{\lambda}{d} r \cos(\phi - \phi_s) = R - \frac{\lambda z}{d} \tan\theta \cos(\phi - \phi_s). \quad (7)$$

Expanding $\tan\theta$ as a power series helps to separate the relevant components of the unknown wavefront. For convenience, θ can be replaced by a dimensionless polar, or radial parameter, ρ, defined as $\rho \equiv \theta/\alpha$;

$$\Delta l = R - \frac{\lambda z}{d}\left(\alpha\rho + \tfrac{1}{3}\alpha^3\rho^3\right)\cos(\phi - \phi_s). \quad (8)$$

Keeping terms up through ρ^3, the path-length difference includes the same spherical component as the original wave, R, plus a linear tilt component related to the grating diffraction "shear" angle. Based on the grating shear angle λ/d, the coefficient $\lambda z/d$ is equivalent to the beam separation s' in the conjugate plane nearest the grating. If this is the image plane, then $s' \equiv s$; for the object plane, s' is related to s by the magnification m, $s' \equiv s/m$. Neglecting the tilt contribution, define the interesting coma term Δl_{grat} as

$$\Delta l_{\text{grat}} = -\tfrac{1}{9} s' \alpha^3 Z_6(\rho, \phi - \phi_s). \quad (9)$$

4.6 Detector tilt or mask-plane tilt

In the absence of re-imaging optics, misalignment of the detector from a plane normal to the central ray can introduce a systematic astigmatic error into the wavefront measurement. The magnitude of this error is easily derived following the arguments presented above for the path-length difference between the test and reference beams.

With a constant z value, Eq. 2 expresses the path-length difference when the detector is aligned normal to the central ray. By allowing z to vary with r and ϕ, describing the detector's tilted plane, the same expression reveals the path-length difference we seek.

An expression for the detector plane, tilted by a small angle τ in an azimuthal direction defined by ϕ_τ is

$$z = z_0 + \tau r \cos(\phi - \phi_\tau). \quad (10)$$

z_0 is the distance from the origin to the detector along the central ray. Equation 10 is inserted into Eq. 2 to derive the new path-length difference $\Delta l'$. The original path-length difference Δl is subtracted from $\Delta l'$ to isolate the detector-tilt astigmatism Δl_{tilt}. As before, we consider terms up through third-order in r and first-order in s.

$$\Delta l_{\text{tilt}} = -\frac{\tau s}{z_0^2} r^2 \cos(\phi - \phi_{\mathbf{s}}) \cos(\phi - \phi_\tau)$$
$$= -\frac{\tau s}{2 z_0^2} \left[r^2 \cos(2\phi - \phi_{\mathbf{s}} - \phi_\tau) + r^2 \cos(\phi_{\mathbf{s}} - \phi_\tau) \right]. \quad (11)$$

Substituting the normalized radius $\rho = r/tz$, Eq. 11 can be written in terms of astigmatism and defocus with piston:

$$\Delta l_{\text{tilt}} = -\tfrac{1}{2} \tau s t^2 Z_4\left(\rho, \phi - \tfrac{1}{2}\left[\phi_{\mathbf{s}} + \phi_\tau\right]\right)$$
$$-\tfrac{1}{4} \tau s t^2 \cos(\phi_{\mathbf{s}} - \phi_\tau) \left[Z_3(\rho, \phi) + Z_0(\rho, \phi) \right]. \quad (12)$$

The magnitude of the systematic error depends on the direction of the tilt (ϕ_τ) relative to the beam-separation direction ($\phi_{\mathbf{s}}$); the error is zero if the detector is tilted about an axis parallel to the beam separation **s**.

4.7 Radial distortion

In the absence of re-imaging optics, the diverging spherical test and reference beams are recorded by a planar detector. In this geometry, the varying solid angle of the detector array introduces a systematic radial distortion. Unlike the systematic errors described above, this radial distortion does not arise from a path-length difference between the test and reference beams. Correcting this distortion, which is very small at low NA values, requires a non-linear adjustment of the radial parameter used in the wavefront analysis.

The radial distortion can be described mathematically via the projection of the spherical coordinate system onto the plane of the detector. Here, the polar angle of a ray in the beam becomes a radial distance from the origin. The wavefront analysis is ultimately performed on a "unit circle" domain in a normalized coordinate system based on the detector array. In this way, rays at the outermost edge of the NA coincide with a unit radius, and the central ray occupies the origin of both coordinate systems.

As before, the distance from the coordinate origin to the detector plane is z, θ is the polar angle, and α is the maximum half-angle within the NA. In the plane of the detector, the normalized radius ρ is related to the spherical coordinate system by

$$\rho(\theta) = \frac{\tan\theta}{\tan\alpha}. \quad (13)$$

Inverting this expression gives θ in terms of the measured coordinate ρ. To facilitate distortion analysis, it is useful to also normalize the polar angle, dividing it by α. The transformed radial coordinate is ρ'.

$$\rho'(\rho) \equiv \frac{\theta(\rho)}{\alpha} = \frac{1}{\alpha} \tan^{-1}(\rho \tan\alpha). \quad (14)$$

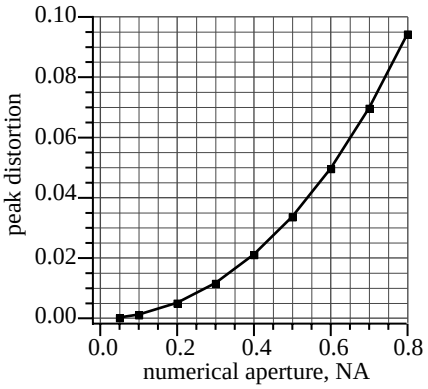

Figure 6. Projection of a spherical beam onto a planar detector causes a radial distortion between the two coordinate systems. The normalized magnitude of the peak radial distortion is shown for a range of NA values.

Incorporating this transformation into the wavefront analysis *before* wavefront fitting to Zernike polynomials is important when the radial distortion is large enough to induce a shear error. Between the two normalized coordinate systems (that of the spherical beam, and that of the measurement), the normalized distortion Δ can be expressed as a function of r:

$$\Delta(\rho) = \rho'(\rho) - \rho = \frac{1}{\alpha} \tan^{-1}(\rho \tan\alpha) - \rho. \quad (15)$$

By definition, these two coordinate systems coincide at the unit radius and at the origin (the distortion is zero at these points). The maximum distortion occurs near ρ equal to 0.5. Values for the peak distortion as a function of NA are plotted in Fig. 6.

4.8 Null test interferometer calibration

The PS/PDI systematic errors described in this chapter are as compensable as they are measurable—except for the radial distortion, which must be removed empirically in the wavefront analysis. Each of the error sources described in Sections 4.4–4.6 depends linearly on the magnitude and direction of beam separation. This fact enables multiple measurements to be combined to isolate the systematic errors attributable to the measurement geometry. While reducing the beam separation does minimize these path-length difference errors, it may not be possible to successfully operate the interferometer with beam separations below approximately 20λ/NA.

An experimental method, the *two-pinhole null test*, has been developed to measure the magnitudes of systematic errors and calibrate the PS/PDI [16, 22, 23]. The null test replaces the image-plane mask window with a second reference pinhole, in a configuration similar to Young's

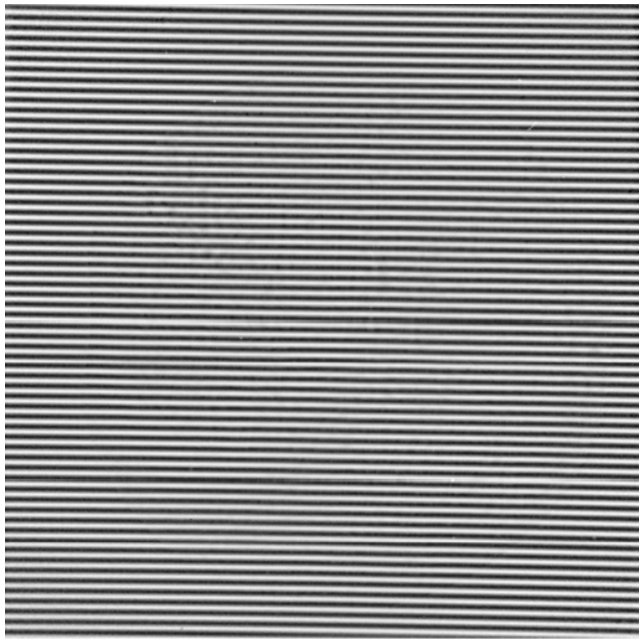

Figure 7. Null test interference pattern from two 100-nm pinholes. Recorded at 13.4-nm wavelength, 0.094 NA (based on the center to edge angle). The detector area is one-square-inch. [From P. Naulleau, *et al.*, Ref. 23]

two-slit experiment. In this way, the interference of two spherical waves is used to simultaneously calibrate the interferometer and probe random error magnitudes.

The null test configuration has been used in the EUV PS/PDI to study the relationship between pinhole size and the quality of the reference wavefront [23]. Additional tests have established beam-alignment tolerances and the opacity of the mask's absorber layer required for adequate spatial filtering.

A typical EUV null test interference pattern is shown in Fig. 7. This pattern was recorded with the EUV PS/PDI configured for the measurement of a 10× Schwarzschild objective. With tilt removed, the geometric coma systematic error is the largest component of the measured wavefront. The Zernike coma coefficient magnitude was 0.415 ± 0.013 nm, within 0.005 nm of its expected value.

4.9 Chromatic properties

One special property of the PS/PDI is its ability to function in the presence of moderately broadband illumination. From a given grating beam splitter position and pitch, the image-plane beam separation is proportional to the wavelength. The fringe density in the detector plane is proportional to the beam separation, and is inversely proportional to the wavelength. In measuring an ideal achromatic system, these two effects balance each other, generating the same fringe pattern for each wavelength component of the illumination.

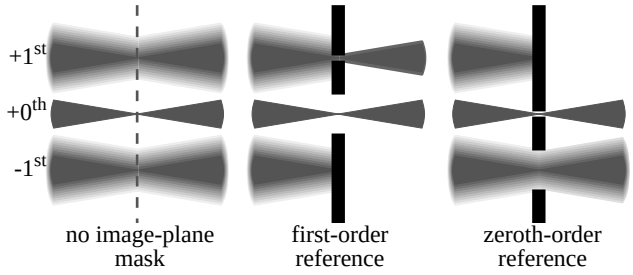

Figure 8. In the presence of moderate bandwidth the positions of first order foci vary with wavelength. This figure illustrates the different chromatic filtering properties of selecting the zeroth or first order as the reference beam. The beams propagate from left to right, and the opaque mask is represented in black. A small, lateral mask translation switches between the two configurations.

The selection of the grating beam splitter's zeroth or first order as the reference beam affects the interferometer's chromatic properties. As stated above, wavelength determines the lateral beam separation in the image plane where the test and reference beams are separated. Specifically, the positions of the zeroth-order foci are the same for each wavelength component, while those of the first order shift with wavelength. In the presence of moderate bandwidth illumination, the first-order foci occupy a range of positions rather than just one point. This is represented in Fig. 8.

If the zeroth-order beam is selected as the reference beam and the reference pinhole is placed at the zeroth-order focus, then the window will transmit a range of first-order wavelength components. On the other hand, if the reference beam is selected from the first-order, then the reference pinhole functions as a monochromator, transmitting the different wavelength components with varying efficiency depending on their focal positions. In the latter case, the test and reference beams may have different chromatic content, thereby reducing the interference fringe contrast. Fringe contrast can be maintained by using the zeroth order as the reference beam.

In the presence of aberrations, chromatic or otherwise, the wavelength independence of the fringe pattern is broken. While the overall fringe density in the pattern of parallel fringes is constant, the aberration-dependent displacement of the fringes is not. The observed pattern represents the incoherent addition of the available wavelength components.

For example, consider an achromatic aberration on a mirror's surface. A localized deviation in the surface figure by height h induces a relative shift in the interference fringe position of h/λ waves. Here, the deviation of the fringes is a wavelength-dependent effect. Yet if the illumination bandwidth is relatively narrow, the intensity distribution is symmetric about a central wavelength, and the detector response is constant over the wavelength range, then it can be shown that the observed fringe pattern is equivalent to the pattern formed by the central wavelength, with a reduced fringe contrast [16].

5. Interferometry

The prototype PS/PDI, developed for the measurement of EUV optics, has been in use since 1996. It uses light from an undulator beamline at the Advanced Light Source at Lawrence Berkeley National Laboratory (LBNL). This work is conducted by members of LBNL's Center for X-Ray Optics, including the author.

To date, five separate 10× Schwarzschild objectives have been studied; two recent wavefront measurements are reported in Fig. 9. These optics, built as part of the ongoing research effort in EUV lithography, demonstrate the fabrication and alignment capabilities that have been achieved. The design specification for the wavefront of these optics is 0.67 nm.

Although PS/PDI wavefront measurements are limited to very high-quality optical systems, and the tolerance on the pinhole positions is beyond the resolution of the optics, the initial alignment of the interferometer's image-plane mask is not difficult. In one strategy, the grating beam splitter is removed and the window is first centered on the test beam. As the mask is translated longitudinally to reach the image plane, the window's edge is used to perform rapid knife-edge beam-width measurements.

5.1 Limitations for large aberrations

The extreme sensitivity and high accuracy of the PS/PDI come at the cost of dynamic range. The interferometer relies on the point-to-point imaging properties of the system under test to produce reference wavefronts of sufficient intensity. If the test optic cannot produce a well-defined point image, the limited size of the window may clip the test beam and the spatial filtering of the reference beam may reduce the contrast of the interference fringes beyond visibility. In general, the reference pinhole must be placed in or near the bright central lobe of the reference beam focal point.

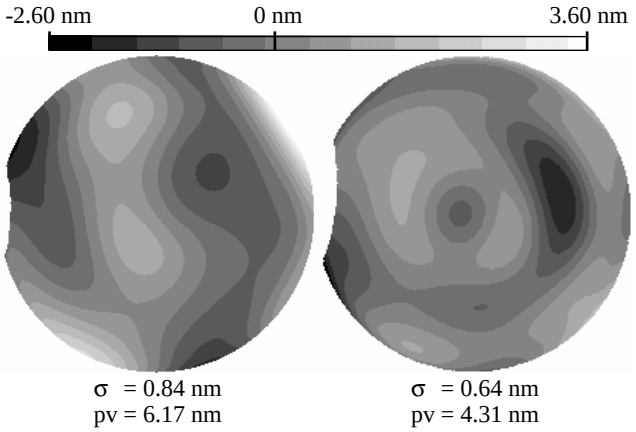

Figure 9. Measured wavefronts from two EUV 10× Schwarzschild objectives fabricated for research in EUV lithography. Recorded by the PS/PDI at 13.4-nm wavelength, with an off-axis, 0.088 NA. The design specification for the wavefront error is 0.67 nm rms. Rays closest to the optic axis are clipped. Grey levels are separated by 0.5 nm. [From K. A. Goldberg, *et al.*, Ref. 24.]

Where significant higher-order aberrations are present, other measurement strategies must be employed. For instance, during the alignment of a compound optical system, interferometry could be performed as a sequential combination of measurements with increasing sensitivity: Foucault knife-edge testing, Ronchi or lateral shearing interferometry, and finally PS/PDI measurements.

For the measurement of mildly aspherical or single-element EUV optics, it may be possible to operate the interferometer at conjugate points where point images *are* formed. A less attractive but potentially viable solution is the incorporation of holographic elements, such as computer-generated holograms (CGH), to null aspherical components of the test wavefront [25]. However, a CGH behaves as an additional reference element, requiring characterization; and to some extent this undoes the benefits of the point-diffraction method of reference wavefront generation.

6. Other applications

The PS/PDI configuration can be used for more than interferometry. With only minor modifications the system is well-suited to the study of optical system characteristics which are of particular interest to EUV lithography: reflectivity, chromatic properties, and flare. These modifications are described in this section.

Using two calibrated photo detectors, the total transmission, or throughput, of the test optic can be characterized. These detectors are usually already required in the design of the interferometer. One detector follows the object plane and is required for the location and adjustment of the object pinhole; the second is the CCD detector, which is used to record interference patterns. While the integrated CCD signal yields the total throughput of the system, spatially resolved information is also available.

Where it is possible to tune the illuminating wavelength (using a monochromator and a broadband, or tunable, EUV source, such as a synchrotron), the combined properties of several reflective multilayer coatings can be studied. These system-level tests have been used to measure the transmission bandwidth and peak-reflectivity wavelength, and to identify defects that are not observable with visible light alone. For example, wavefront measurements performed over a range of wavelengths have been used to study chromatic aberrations in a two-mirror EUV objective. [26]

Another parameter of great concern for lithography is flare, the undesired distribution of power in the vicinity (within a few microns) of bright image features. Flare is caused by mid- and high-spatial-frequency roughness in optical substrates or coatings. As a result of the short

wavelength of EUV light compared with wavelengths used in today's optical lithography (248 nm, 193 nm, etc.), EUV systems are more susceptible to flare. For this reason, during fabrication great emphasis is placed on the finish as well as the figure of optical substrates used as EUV mirrors.

While imaging provides the ultimate measurement of flare, the PS/PDI enables at least two different system-level flare tests. The mid-spatial-frequency range of optical aberrations, the range most important to flare, is the most difficult to measure. In collaboration with other at-wavelength and auxiliary flare measuring techniques performed on the individual optical elements (white-light interferometry, EUV scatterometry [27], atomic-force microscopy, etc.) the PS/PDI tests fill in this important range of power spectral density (PSD) measurement.

One PS/PDI flare measurement is similar to a knife-edge test, and can be performed with a minor modification to the PS/PDI image-plane mask [28]. From a single point object, the power radiated into the field of view is measured using a detector and an appropriately-sized large window in the image plane. Measurements are made as the window's edge is translated across the focused beam. Analysis reveals the position-dependent fraction of the total power that falls outside of the focused beam.

A second at-wavelength flare measurement technique uses elongated image-plane mask windows to extend the spatial-frequency resolution of the PS/PDI into the range of mid-spatial-frequencies [28]. The point-spread function (PSF) of the optic can be measured interferometrically as part of the standard wavefront measurements. The flare can be predicted by combining these low- and mid-spatial-frequency PSF measurements with the high-frequency power spectrum measured in other ways.

7. Future directions

In use for several years, and successfully applied to the measurement of several prototype EUV lithographic optics, the PS/PDI has demonstrated its usefulness, its accuracy, and its potential. Undoubtedly, the most significant challenges await the development of optical systems not yet conceived. With higher numerical aperture and shorter wavelength, the extension of diffraction-based interferometric techniques is not guaranteed.

For application in large-scale production environments, and where source brightness limits the coherent EUV power available to interferometry, the role of at-wavelength testing, and point diffraction interferometry in particular, must be carefully studied. In collaboration with other techniques, the PS/PDI may become an essential tool; or it may be relegated to the role of gold standard used in the calibration of other interferometries. Alternatively, it may be applied in the development of reference optics that are used in other testing strategies.

8. Acknowledgments

I wish to thank Hector Medecki, Jeffrey Bokor, Patrick Naulleau, and Edita Tejnil, whose innumerable contributions have been instrumental to the genesis and development of this work, and Gary Sommargren for insightful input throughout. Experimental research in EUV interferometry is performed by members of the Center for X-Ray Optics at Lawrence Berkeley National Laboratory. This research has been supported by the Extreme Ultraviolet Limited Liability Company (EUV LLC), the Semiconductor Research Corporation, the DARPA Advanced Lithography Program, and by the Office of Basic Energy Sciences of the U.S. Department of Energy.

9. References

1. M. D. Himel, "Optic fabrication and metrology for soft x-ray projection lithography," in OSA Proceedings on Soft X-Ray Projection Lithography, Vol. 18, A. M. Hawryluk and R. H. Stulen, Eds., Optical Society of America, Washington, D.C., 1993, pp. 108-9.
2. D. M. Williamson, "The elusive diffraction limit," in OSA Proceedings on Extreme Ultraviolet Lithography, Vol. 23, F. Zernike and D. T. Attwood, Eds., Optical Society of America, Washington, D.C., 1994, pp. 68-76.
3. G. E. Sommargren, "Phase shifting diffraction interferometry for measuring extreme ultraviolet optics," in OSA Trends in Optics and Photonics, Vol. 4, Extreme Ultraviolet Lithography, G. D. Kubiak and D. R. Kania, Eds., Optical Society of America, Washington, D.C., 1996, pp. 108-12.
4. G. E. Sommargren, "Diffraction methods raise interferometer accuracy," Laser Focus World, **32** (8), 61-71 (1996).
5. L. M. Foucault, "Description des procedees employes pour reconnaitre la configuration des surfaces optiques," C. R. Acad. Sci. (Paris), **47**, 958 (1858).
6. V. Ronchi, "Due Nuovi Metodi per lo Studio delle Superficie e die Sistemi Ottici," Ann. Sc. Norm. Super. Pisa, **15**, (1923).
7. A. K. Ray-Chaudhuri, W. Ng, F. Cerrina, *et al.*, "Alignment of a multilayer-coated imaging system using extreme ultraviolet Foucault and Ronchi interferometric testing," Journal of Vacuum Science & Technology B, **13** (6), 3089-93 (1995).
8. A. K. Ray-Chaudhuri, K. D. Krenz, R. P. Nissen, *et al.*, "Initial results from an extreme ultraviolet interferometer operating with a compact laser plasma source," Journal of Vacuum Science & Technology B, **14** (6), 3964-8 (1996).
9. J. E. Bjorkholm, A. A. MacDowell, O. R. Wood II, Z. Tan, *et al.*, "Phase-measuring interferometry using extreme ultraviolet radiation," Journal of Vacuum

Science & Technology B, **13** (6), 2919-22 (1995).
10. W. P. Linnik, “A simple interferometer for the investigation of optical systems,” Proceedings of the Academy of Sciences of the USSR, **1**, 208 (1933).
11. R. N. Smartt and W. H. Steel, “Theory and application of point-diffraction interferometers (telescope testing),” Japanese Journal of Applied Physics, **14** (Suppl. **14-1**), 351 (1975).
12. K. A. Goldberg, R. Beguiristain, J. Bokor, *et al.*, “Progress towards λ/20 extreme ultraviolet interferometry,” Journal of Vacuum Science & Technology B, **13** (6), 2923-27 (1995).
13. H. Medecki, E. Tejnil, K. A. Goldberg, and J. Bokor, “Phase-shifting point diffraction interferometer,” Optics Letters, **21** (19), 1526-28 (1996).
14. P. Naulleau, K. A. Goldberg, E. Tejnil “Phase-shifting point diffraction interferometer grating designs,” *Patent pending*.
15. P. Naulleau, K. A. Goldberg, “Dual-domain point diffraction interferometer,” *submitted to Applied Optics*, August, 1998.
16. K. A. Goldberg, “Extreme Ultraviolet Interferometry,” Ph.D. dissertation, (U. California, Berkeley, 1997).
17. H. Medecki, U.S. Patent 5,835,217: “Phase-shifting point diffraction interferometer,” (Nov. 1998).
18. A. B. Bathia and E. Wolf, “The Zernike circle polynomials occurring in diffraction theory,” Proc. Phys. Soc., **B65**, 909-10 (1952).
19. D. J. Fischer, J. T. O’Bryan, *et al.*, “Vector formulation for interferogram surface fitting,” Applied Optics, **32** (25), 4738-43 (1993).
20. J. Y. Wang and D. E. Silva, “Wave-front interpretation with Zernike polynomials,” Applied Optics, **19** (9), 1510-18 (1980).
21. A. Babinet, Compt. Rend., **4**, 638ff (1837).
22. K. A. Goldberg, E. Tejnil, S. H. Lee, “Characterization of an EUV Schwarzschild objective using phase-shifting point diffraction interferometry,” Proc. SPIE, **3048**, 264-70 (1997).
23. P. Naulleau, K. A. Goldberg, S. H. Lee, *et al.*, “Characterization of the accuracy of EUV phase-shifting point diffraction interferometry,” in Emerging Lithographic Technologies II, Y. Vladimirski, ed., Proc. SPIE, **3331**, 114-23 (1998).
24. K. A. Goldberg, P. Naulleau, R Gaughan, H. Chapman, J. Goldsmith, and J. Bokor., “Direct comparison of EUV and visible-light interferometries,” in Emerging Lithographic Technologies III, Proc. SPIE, **3676**, (1999), *to be published.*
25. A. J. MacGovern, J. C. Wyant, “Computer generated holograms for testing optical elements,” Applied Optics, **10** (3), 619-24 (1971).
26. E. Tejnil, K. A. Goldberg, J. Bokor, “Phase effects owing to multilayer coatings in a two-mirror extreme ultraviolet Schwarzschild objective,” Applied Optics, **37** (34), 8021-9 (1998)
27. E. M. Gullikson, “Scattering from normal incidence EUV optics,” in Emerging Lithographic Technologies II, Y. Vladimirski, ed., Proc. SPIE, **3331**, 72-80 (1998).
28. P. Naulleau, E. M. Gullikson, K. A. Goldberg, (unpublished).